Boosting the Catalytic Activity and Stability of Ru Metal Clusters in Hydrodeoxygenation of Guaiacol through MWW Zeolite Pore Constraints

Ping He, Qisong Yi, Huawei Geng, Yuanchao Shao, Meng Liu, Zhijie Wu, Wenhao Luo, Yuanshuai Liu, Valentin Valtchev

Boosting the catalytic activity and stability of Ru metal clusters in hydrodeoxygenation of guaiacol through MWW zeolite pore constraints

Ping He,[1] Qisong Yi,[1] Huawei Geng,[1] Yuanchao Shao,[1] Meng Liu,[3] Zhijie Wu,[3] Wenhao Luo,[4] Yuanshuai Liu,[1*] Valentin Valtchev[1, 2*]

[1]Qingdao Institute of Bioenergy and Bioprocess Technology, Chinese Academy of Sciences, Songling Road 189, Laoshan District, Qingdao, 266101, China

[2]Laboratoire Catalyse et Spectrochimie, Normandie Univ, ENSICAEN, UNICAEN, CNRS, 6 boulevard Maréchal Juin, 14050 Caen, France

[3]State Key Laboratory of Heavy Oil Processing and the Key Laboratory of Catalysis of CNPC, China University of Petroleum-Beijing, Fuxue Road 18, Changping, Beijing, 102249, China

[4]CAS Key Laboratory of Science and Technology on Applied Catalysis, Dalian Institute of Chemical Physics, Chinese Academy of Sciences, 457 Zhongshan Road, Dalian, 116023, China

ABSTRACT

The liquid-phase hydrodeoxygenation (HDO), catalyzed by metal or metal-acid sites, provides an effective catalytic strategy to remove oxygen-containing functionalities of lignin-derived phenolic compounds on the route to fuels and chemicals. Developing the catalyst with high activity and stability is crucial for such a chemical process but still remains a significant challenge. In this contribution, highly dispersed subnanometric Ru metal clusters (< 1.5 nm) encapsulated in the cavities of MWW zeolites, including MCM-22 and its siliceous analog ITQ-1, have been developed for the HDO of guaiacol, an important lignin-derived phenolic monomer, in an apolar liquid phase under mild conditions (160°C, 3 MPa H_2). We validate the effective encapsulation of Ru metal clusters in ITQ-1 and HMCM-22 zeolites cavities via complementary characterization methods. The detailed reaction pathways of the HDO of guaiacol are depicted by using guaiacol, phenol, and anisole as reactants. The subnanometric Ru metal clusters confined in MWW zeolite thin layers (20-30 nm in thickness) show remarkable enhancement in HDO activity compared to the large metal particles. The close proximity between Ru metal clusters and Brønsted acid sites (BAS) confined in zeolite constraints delivers a synergistic effect, leading to an additional enhancement in catalytic activity as well as product selectivity. The super stability of the ultrafine Ru metal clusters against sintering and leaching after successive catalytic runs is achieved. The well-defined mono- or bi-functional Ru-containing MWW zeolite catalysts enable the fundamental understanding of HDO of lignin-derived phenolic compounds in the apolar liquid phase and

also provide a prototype for the design of superior catalysts for the other energy-related transformations.

Keywords: *Biomass; Guaiacol; Hydrodeoxygenation; Bi-functional catalyst; Metal clusters*

1. INTRODUCTION

The efficient utilization of lignocellulosic biomass is of great importance in pursuing a sustainable future for producing fuels, chemicals, and materials. Compared to cellulose and hemicellulose, which have been intensively investigated and profitably developed in the past decades, value-added applications of lignin are very limited in current biorefineries. Within this context, "Lignin-First Biorefinery" is an attractive opportunity to augment the sustainability of biorefinery through the catalytic valorization of native lignin to the lignin-derived bio-oils in the first step.[1-3] Such bio-oils can serve as a platform for a broad range of bio-based products via the subsequent catalytic routes.[4-6] In terms of oxygen-free transportation fuel production, bi-functionally catalyzed hydrodeoxygenation (HDO) has been approved as a valid method for oxygen removal of bio-oils to saturated hydrocarbon under mild conditions in the liquid phase.[7, 8]

Guaiacol, one of the most abundant lignin depolymerization products,[9] has been extensively adopted as a model compound to mimic the real lignin-derived bio-oils for the liquid-phase HDO investigations. Conceptually, three types of C-O bonds in guaiacol, i.e., C_{aryl}-OH, C_{alkyl}-OAr, and C_{aryl}-OCH_3, can be cleaved via hydrogenolysis over metal moieties or by hydrolysis on acid sites, or through the cascade hydrogenation-dehydration reactions over a metal/acid bi-functional catalyst. Noble metals such as Pt, Pd, Ru, etc., have been widely employed in the HDO of guaiacol owing to their excellent hydrogenation and hydrogenolysis activity.[10-15] Among them, the Ru-based catalysts show a higher selectivity towards cyclohexane than the other metal-based catalysts.[16-18] As a typical solid acid with versatile applications in petrochemistry, zeolites such as MFI, BEA, FAU, etc., also remain an inspiring presence in the context of biomass valorization.[19, 20] The structural and physicochemical properties of zeolites are able to provide spatial restriction for the ultra-small metal clusters (< 2 nm) formation, subsequently boosting the thermal and hydrothermal stability and sometimes the catalytic activity of the metal species.[21-25] Unavoidably, the micropores of zeolites, to some extent, may block the accessibility of the larger molecules to the internal acid sites as well as the confined metal clusters due to steric restrictions. Consequently, nanosized or nanosheet-like zeolites have been developed to enhance the mass transport of bulky reactant molecules.[26-32] However, the synthesis of nanosized or nanosheet-like zeolites usually requires specific synthesis conditions

or complex product processing, hampering their practical applications. MWW type zeolites, a unique class of layered zeolites, composed of stacked ultrathin single-unit-cell layers (ca. 2.5 nm in thickness) which has been successfully used for aromatic alkylation,[33, 34] by contrast, can be facilely synthesized with the conventional hydrothermal method. Owing to their inherent superiority in mass transport for bulky molecules, MWW type zeolites are expected to be promising catalytic materials for the HDO of lignin-derived phenolic monomers.

In this contribution, highly dispersed subnanometric Ru metal clusters (< 1.5 nm) encapsulated in MWW zeolites, including MCM-22 and its siliceous analog ITQ-1, have been developed by *in situ* ligand-stabilized hydrothermal crystallizations.[35-37] We demonstrate that Ru metal clusters are successfully encapsulated in the MWW zeolite cavities via complementary characterization methods. The MWW zeolite thin layers with 20-30 nm thickness lead to improved accessibility of Ru metal clusters confined in zeolite cavities and subsequently realize a much higher HDO activity of guaiacol under mild reaction conditions (160°C, 3 MPa H_2). In addition, the well-defined Ru metal clusters with comparable size distribution and identical chemical states allow unraveling more clearly the synergistic roles of metal and acid sites on reaction pathways, reaction rates, and product selectivity in the HDO of guaiacol. Besides the enhanced activity of Ru metal clusters, encapsulation of Ru in MWW zeolite also leads to significantly improved catalyst stability during HDO reactions. These findings provide insights into the fundamental understanding of HDO of guaiacol and afford a practical approach for the design of catalysts with excellent performances for the valorization of lignin-derived phenolic compounds.

2. EXPERIMENTAL

2.1 Chemicals

All reagents were purchased from commercial suppliers and used without further purification: N, N, N-Trimethyl-1-adamantylammonium hydroxide ($TMAda^+OH$, Macklin, 25% in water), Hexamethyleneimine (HMI, J&K chemicals, > 98%), Fumed silica (Macklin, 99.8%), Silica sol (Macklin, 29~31%), Sodium aluminate ($NaAlO_2$, Sigma-Aldrich, Al_2O_3: 50-56%, Na_2O: 37-45%), Ruthenium (III) chloride ($RuCl_3 \cdot H_2O$, Macklin, 99.8%), Ethylenediamine (En, Sinopharm chemical, ≥ 99.0%), Sodium hydroxide (NaOH, Sinopharm chemical), Sodium chloride (NaCl, Sinopharm chemical), Phenol (Aladdin, ≥ 99.0%), Guaiacol (Aladdin, 99%), Anisole (Aladdin, 99.7%), Dodecane (Aladdin, > 99.0%). Deionized water was produced by a Milli-Q integral ultrapure water system.

2.2 Materials synthesis

Synthesis of ITQ-1. ITQ-1 layered precursor, ITQ-1(P), was synthesized using $TMAda^+OH$ and HMI as co-structure-directing agents, where P is used to denote layered precursors that are not covalently connected. The precursor gel with a composition of $1SiO_2$: 0.2NaCl: $0.25TMAda^+OH$: 0.31HMI: $44H_2O$ was prepared. In a typical synthesis, 0.36 g NaCl was first dissolved in 16.5 g H_2O, followed by adding 6.49 g $TMAda^+OH$ and 0.96 g HMI under stirring for 1h. 1.84 g fumed silica was then added to the mixture. After vigorous stirring overnight, the gel was aged in a 50 mL PTFE-lined stainless-steel autoclave at 80℃ for 12 h, and then heated to 150℃ for 120 h with a rotation at 60 rpm. The obtained product was collected by centrifuge and washed with deionized water until a near-neutral pH, dried overnight at 80°C, and labeled as ITQ-1(P). ITQ-1 was obtained via calcination of ITQ-1(P) at 550°C in the air for 6 h, during which the organic template was removed, and the silanol groups on adjacent lamellar condensed.

Synthesis of (H)MCM-22. MCM-22 precursor, MCM-22(P), was synthesized under hydrothermal conditions. Typically, 0.18 g $NaAlO_2$ and 0.12 g NaOH were dissolved in 20.54 g deionized water, followed by adding 1.52 g HMI. Subsequently, 6.15 g silica sol was added dropwise to obtain a gel of $1SiO_2$: $0.033Al_2O_3$: $0.09Na_2O$: 0.5HMI: $44.9H_2O$. After stirring for 3 h at room temperature, the homogeneous gel was aged in a 50 mL PTFE-lined stainless-steel autoclave at 80℃ for 12 h, then heated at 160℃ for 120 h with a rotation at 60 rpm. The products were collected by centrifuge and washed with deionized water until a near-neutral pH, dried overnight at 80°C, and labeled as MCM-22(P). MCM-22 was obtained via the calcination of MCM-22(P) at 550°C in the air for 6 h. H-type MCM-22, denoted as HMCM-22, was obtained by the ion-exchange of MCM-22 twice in 0.3 M ammonium acetate solution under stirring at 60°C for 2 h, and then dried overnight at 80°C, followed by the calcination at 450°C for 6 h.

Synthesis of Ru@ITQ-1-IN, Ru@HMCM-22-IN, *Ru@ITQ-1-IN(S)* and *Ru@HMCM-22-IN(S)*. Ru-containing MWW zeolites were prepared through the *in situ* hydrothermal crystallization method, described elsewhere.[36] Ethylenediamine was applied to react with $RuCl_3$ (with ethylenediamine/Ru molar ratio of 13) overnight at room temperature in the aqueous phase to form Ru-ethylenediamine complexes. Typically, 37.8 mg $RuCl_3 \cdot H_2O$ was dissolved in 2.5 g water, then 400 ul ethylenediamine (En) was added and fully stirred to prepare Ru^{3+}-En complexing solution. The complexing solution was added to the initial gel of ITQ-1 (P) and MCM-22 (P) and fully stirred. After mixing for 2 hours, the metal-containing gel was transferred into an autoclave with the same heating condition used for the synthesis of ITO-1(P) and MCM-22(P) with a rotation speed of 60 rpm or 0 rpm (static). The product was collected by centrifuge, washed with deionized water and acetone, and dried overnight at 80℃. Ru@ITQ-

1 and Ru@MCM-22 were obtained by the calcination of Ru@ITQ-1(P) and Ru@MCM-22(P) in the air at 550°C for 6 h with a ramping rate of 1°C min^{-1}. The bi-functional catalyst, Ru@HMCM-22 was obtained by the ion-exchange of Ru@MCM-22 in ammonium acetate solution under the conditions described above. Catalysts synthesized with 60 rpm and 0 rpm are denoted respectively as Ru@ITQ-1-IN or Ru@HMCM-22-IN, and Ru@ITQ-1-IN(S) or Ru@HMCM-22-IN(S).

Preparation of Ru@ITQ-1-imp and Ru@HMCM-22-imp. Ru@ITQ-1-imp and Ru@HMCM-22-imp were prepared by an incipient-wetness impregnation method. Typically, a given amount of $RuCl_3$ aqueous solution was mixed with the zeolite powder and kept at room temperature for 12 h. The samples were then dried at 80°C overnight and calcined in airflow at 550°C (ramping rate: 1°C min^{-1}) for 6 h.

2.3 Catalysts characterization

Powder X-ray diffraction (XRD) analysis was performed on a Rigaku SmartLab diffractometer using Cu Kα radiation at 40 kV and 150 mA. SiO_2/Al_2O_3 ratios were determined on a Rigaku ZSX Primus X-ray fluorescence (XRF) spectrometer. Scanning electron microscopy (SEM) images were obtained on a Hitachi S-4800 instrument. Transmission electron microscopy (TEM) and scanning transmission electron microscopy (STEM) in the high angle annular dark field mode (HAADF-STEM) were carried out on a JEM-2100 microscope at 200 kV. The elemental composition and distribution were analyzed by an energy-dispersive X-ray spectrometer. The BET specific surface area and pore volume were determined by N_2 adsorption-desorption isotherms measured at -196°C using a Micromeritics ASAP 2460 volumetric adsorption analyzer. The metal loading of catalysts was measured by inductively coupled plasma-optical emission spectroscopy (ICP-OES, Agilent 730 instrument).

The IR spectra of adsorbed pyridine were recorded on a Perkin-Elmer 2000 spectrometer at a resolution of 4 cm^{-1}. The sample was loaded as a self-supporting wafer and activated in a vacuum (p = 10^{-6} mbar) at 450°C for 1 h with a heating rate of 10°C min^{-1}. After cooling to 150°C, the sample was equilibrated with 0.1 mbar of pyridine for 30 min followed by outgassing for 1 h, after which a spectrum with the chemisorbed pyridine was recorded. The concentrations of Brønsted and Lewis acid sites were calculated from the integral intensities of the peaks at 1540 and 1450 cm^{-1}, respectively, in the IR spectra of adsorbed pyridine.

X-ray photoelectron spectroscopy (XPS) measurements were performed on a Thermo ESCALAB 250Xi apparatus. Spectra were obtained using an aluminum anode (Al Ka = 1486.6 eV) operating at a spot size of 500 μm. Survey scans were measured at constant pass energy of

100 eV with an energy step size of 1.0 eV, and more detailed region scans at pass energy of 20 eV with an energy step size of 0.05 eV. The correction was performed with a peak at C 1s at 284.80 eV.

Hydrogen chemisorption was conducted to determine the dispersion of Ru clusters. Samples were first reduced at 350°C in pure H_2 at a ramping rate of 2°C min^{-1} and then kept in a dynamic vacuum at 300°C for 1 h. Hydrogen adsorption isotherms were measured at 40°C and 5.0-50 kPa of H_2 for the samples. Ru metal dispersions (D) were calculated by assuming $H/Ru_s = 2$. The mean cluster diameter was estimated from the metal dispersion using $d_{chem} = 6v_m/a_mD$, where v_m is the volume occupied by an atom in bulk metal ($v_{Ru} = 13.65\times10^{-3}$ nm^3), a_m is the area occupied by a surface atom ($a_{Ru} = 6.35\times10^{-2}$ nm^2).[38]

2.4 Catalytic reactions

All experiments were conducted in a stirred batch reactor (Parr reactor, Series 4843, 300 mL). Typically, 0.3-1.0 g reactants (e.g., guaiacol, phenol, or anisole) and the catalysts were mixed with 100 mL dodecane in the autoclave. After loading the mixture, the reactor was flushed with 2 MPa H_2 three times, charged with 3 MPa H_2, and then heated up to 160°C. The time at which the temperature reached the set point was taken as time zero. The stirring speed was kept at 700 rpm from the beginning of the heat-up period. The figure captions, and table footnotes provide detailed descriptions of reaction conditions. Samples were taken at fixed time intervals and analyzed on a gas chromatograph (with a 30 m × 250 μm HP-5 capillary column and flame ionization detector) combined with a mass spectrometer (GC-MS, Shimadzu QP 2010SE). The conversion and yield were calculated on a carbon mole basis. Conversion = (weight of converted reactant/weight of the starting reactant) × 100%. Selectivity of liquid products (C%) = (C atoms in the appointed product/C atoms in all liquid products) × 100%.

3. RESULTS AND DISCUSSION

3.1 Characteristic evidence for encapsulation of Ru metal clusters in MWW zeolites prepared by *in situ* crystallization.

The main physicochemical properties of the studied materials have been compiled in **Figure 1** and **Table 1**, and the other characterization results can be found in the Supplementary Information (**Table S1** and **Figures S1-S7)**. ITQ-1 and HMCM-22, as well as the Ru-containing zeolites synthesized by *in situ* crystallization method, i.e., Ru@ITQ-1-IN, Ru@HMCM-22-IN, Ru@ITQ-1-IN(S) and Ru@HMCM-22-IN(S), showed characteristic peaks of the MWW structure, according to the XRD patterns (**Figure 1a** and **Figure S1**). The absence of diffraction

peaks corresponding to the metallic or oxide Ru indicates no formation of large metal crystals in four Ru-containing samples. Compared to ITQ-1 and HMCM-22, a slightly lower X-ray zeolite crystallinity for Ru@ITQ-1-IN and Ru@HMCM-22-IN was observed, which might originate from the partial collapse of the zeolite structure owing to the metal entrance. SEM (**Figure S2**) and TEM (**Figure 1b**) images revealed that both Ru@ITQ-1-IN and Ru@HMCM-22-IN samples showed a typical nanosheet-like (with a thickness of 20-30 nm) morphology. HADDF-STEM images and EDX-mapping results, revealed a homogeneous distribution of subnanometric Ru clusters with a mean diameter of 1.2-1.3 nm over Ru-containing MWW zeolites (**Figures 1b** and **1c**). The chemical state of Ru was studied via the Ru $3d_{5/2}$ XPS due to the overlap of the Ru $3d_{3/2}$ signals with the C 1s sample holder (**Figure S3**). For Ru@ITQ-1-IN and Ru@HMCM-22-IN, the XPS analysis showed the same peak at 280.7 eV assigned to the presence of Ru^{4+}species,[39] indicative of the formation of Ru metal oxides (RuO_2) with the identical oxidation states upon the calcination in the airflow under 550°C for two catalysts (see Experimental section).

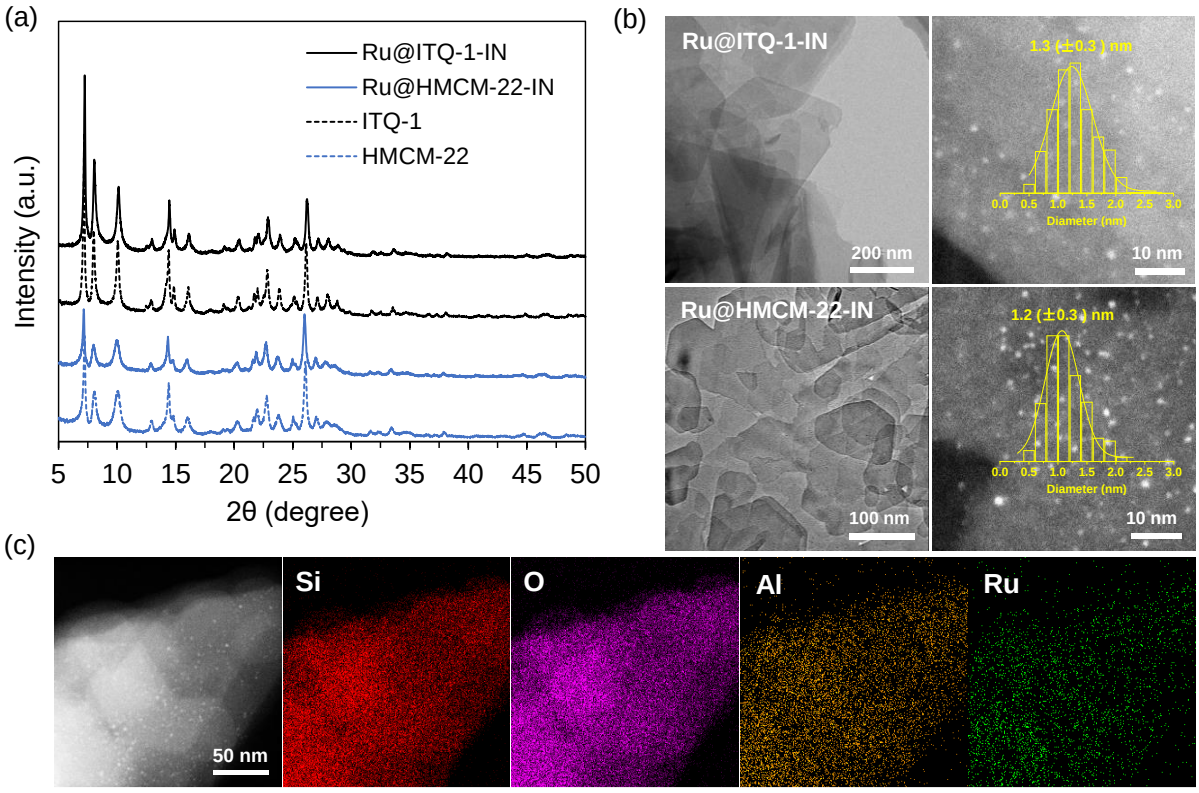

Figure 1. (a) XRD patterns of the parent and Ru-containing MWW zeolites; (b) TEM and HADDF-STEM images of the Ru@ITQ-1-IN and Ru@HMCM-22-IN; (c) TEM and HADDF-STEM images of the Ru@HMCM-22-IN catalyst with the elemental mapping of Si, O, Al, and Ru by EDX; Ru metal particle size distributions in (b) were obtained by counting more than 200 particles on each sample. Note that all samples were calcined before the measurements.

To validate the encapsulation of Ru metal clusters in Ru@ITQ-1-IN and Ru@HMCM-22-IN, two reference samples with similar Ru metal loading were prepared via the incipient-wetness impregnation method, i.e., Ru@ITQ-1-imp and Ru@HMCM-22-imp. Unlike the *in situ* synthesized samples, Ru@ITQ-1-imp and Ru@HMCM-22-imp showed distinct peaks of RuO_2 (110) and RuO_2 (101) at the diffraction angle (2θ) of ~ 29° and ~ 33°, respectively (**Figure S4**), indicating the formation of large metal particles on the external surface of zeolites. TEM results also revealed the randomly distributed large Ru metal particles, with the size ranging from 1-40 nm, supported on two impregnated samples (**Figure S5**). The structural properties of the two impregnated samples, as revealed by N_2 adsorption and desorption results (**Figure S6**), were nearly identical to the parent ITQ-1 and HMCM-22 zeolites, whereas the microporous surface area and volume decreased significantly on Ru@ITQ-1-IN and Ru@HMCM-22-IN samples (**Table 1**). The slight loss of crystallinity (**Figure 1a**) together with the significant decrease in microporous surface area and porosity suggested the effective encapsulation of Ru clusters into MWW zeolites, although they already exceeded the size of MWW supercage (0.71 nm × 0.71 nm × 1.81 nm).[40-42] The size and dispersion of Ru metal clusters on the impregnated and *in situ* synthesized samples were also assessed by H_2 chemisorption. Compared to Ru@ITQ-1-imp and Ru@HMCM-22-imp, Ru metal clusters with size at subnanometric level ($\leqslant$ 1.5 nm) and high dispersions ($\geqslant$ 86%) were observed for Ru@ITQ-1-IN and Ru@HMCM-22-IN samples (**Table 1**), proving again the superiority of *in situ* synthesis method for the encapsulation of metals into zeolites.

Table 1. Physicochemical properties of pristine zeolite materials and Ru containing zeolite catalysts.

Samples	SiO_2/Al_2O_3[a]	Ru Loading (wt %)[b]	D[c]	d_{chem} (nm)[c]	BET surface area ($m^2\ g^{-1}$)[d]			Pore volume ($cm^3\ g^{-1}$)[d]		
					Micro	Meso	Total	Micro	Meso	Total
ITQ-1	N.A.	N.A.	N.A.	N.A.	431.9	110.6	542.5	0.17	0.24	0.41
Ru@ITQ-1-IN	N.A.	0.15	0.86	1.5	362.0	128.1	490.1	0.14	0.26	0.40
Ru@ITQ-1-IN(S)	N.A.	0.17	0.84	1.5	325.8	69.1	398	0.12	0.16	0.28
Ru@ITQ-1-imp	N.A.	0.14	0.28	4.6	387.4	119.0	506.4	0.16	0.15	0.31
HMCM-22	25	N.A.	N.A.	N.A.	455.1	180.1	635.2	0.18	0.49	0.67
Ru@HMCM-22-IN	24	0.34	0.92	1.4	376.2	191.7	567.9	0.15	0.47	0.62

Ru@HMCM-22-IN(S)	27	0.38	0.85	1.5	326	86.6	412.6	0.13	0.19	0.32
Ru@HMCM-22-imp	25	0.31	0.47	2.7	436.2	183.2	619.4	0.17	0.48	0.65

[a] Determined by XRF; [b] Determined by ICP-OES; [c]Ru dispersion and the mean particle diameter is determined by H_2 chemisorption; [d] The specific surface areas and pore volumes are determined by N_2 adsorption-desorption analysis at -196°C. The specific surface area is obtained by the BET method; Micropore surface area and micropore volume are calculated by the t-plot method; Mesopore volume is calculated by subtracting the micropore volume from the total volume.

The acidic properties of parent HMCM-22 and Ru-containing zeolites were probed by Py-IR (**Table S1**). After the incipient-wetness impregnation of Ru, the BAS concentration of HMCM-22 decreased from 0.81 to 0.71 mmol g^{-1}, while the concentration of Lewis acid sites (LAS) increased from 0.43 to 0.72 mmol g^{-1}. The additional LAS stem from the Ru metal oxides, which partially interacted with the zeolite acidic hydroxyl groups and reduced BAS concentration. The change of acidity was more pronounced for Ru@HMCM-22-IN samples. For instance, the BAS concentration of Ru@HMCM-22-IN (0.44 mmol g^{-1}) dropped by almost half compared to the parent HMCM-22. Note that the Ru metal loading and SiO_2/Al_2O_3 ratio (see **Table 1**) were comparable for Ru@HMCM-22-imp and Ru@HMCM-22-IN samples, the remarkable decrease of BAS on Ru@HMCM-22-IN is thus an additional indication of the successful encapsulation of a large portion of Ru metal clusters into zeolite cavities.

3.2 Improving the accessibility of Ru metal clusters encapsulated in MWW zeolite nanosheets.

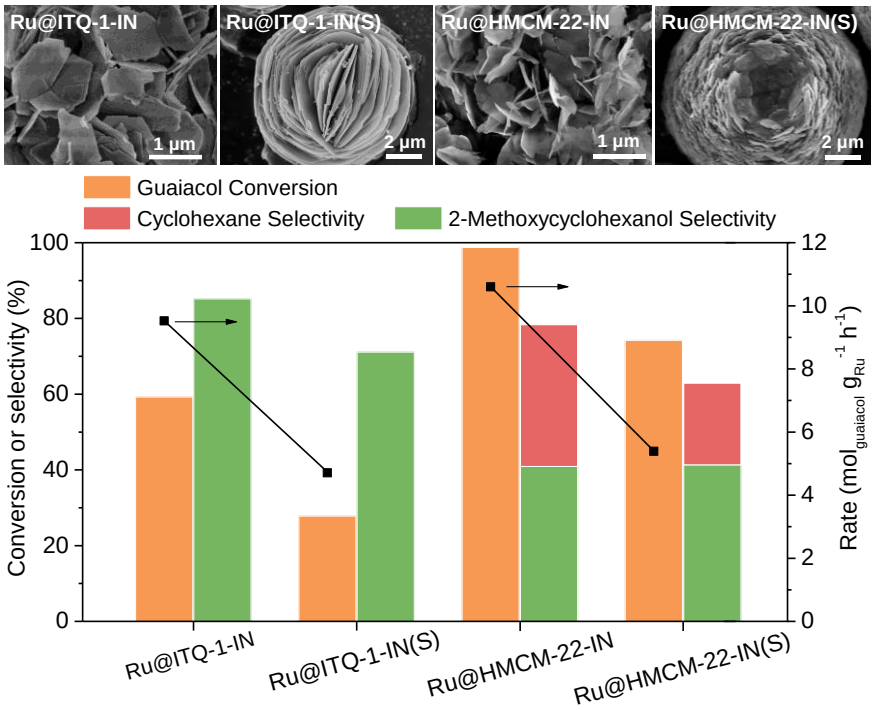

Figure 2. Catalytic performance of Ru-containing MWW zeolites in HDO of guaiacol. Ru@ITQ-1-IN and Ru@HMCM-22-IN were synthesized at rotation speed of 60 rpm; Ru@ITQ-1-IN(S) and Ru@HMCM-22-IN(S) were synthesized at rotation speed of 0 rpm. Guaiacol conversion, products selectivity and reaction rates were calculated at the reaction time of 60 min over the applied catalysts. Reaction conditions: 0.30 g guaiacol, 0.10 g catalyst, 100 mL dodecane, 3 MPa H_2 (ambient temperature), stirred at 700 rpm, 160°C.

In general, MWW zeolite can be synthesized under static or agitation conditions, whereas agitation is able to prevent the excessive aggregation of zeolite platelets into lamellar particles.[43] In the present work, Ru-containing ITQ-1 and HMCM-22 with identical metal loading and comparable cluster size (see **Table 1** and **Figure S7**) synthesized under static (0 rpm) and agitation (60 rpm) conditions were applied to elucidate the impact of zeolite morphology in the HDO of guaiacol. Compared to Ru@ITQ-1-IN and Ru@HMCM-22-IN in the form of well-dispersed nanosheets (i.e., ≤ 1 μm in diameter, 20-30 nm in thickness), Ru@ITQ-1-IN(S) and Ru@HMCM-22-IN(S) prepared under static conditions are the round lamellar particles (8-10 μm in diameter) composed of aggregated thicker (50-100 nm) zeolite platelets (see **Figures 2** and **S2**). The dense stacking of thicker and larger zeolite platelets leads to the significantly reduced specific surface area and the pore volume (**Table 1**), and hence results in decreased reaction rates, as well as the selectivity of primary products, i.e., cyclic alcohols and cyclohexane, in the HDO of guaiacol (**Figure 2**).

The enhanced catalytic performance of Ru@ITQ-1-IN and Ru@HMCM-22-IN was first caused by the higher surface area providing more exposed active sites for guaiacol. In addition, the much thinner zeolite nanosheets composed of about 10 single MWW layers (with a thickness

of ca. 2.5 nm) minimized the diffusion limitations within the catalyst and thus afforded more accessible Ru metal clusters for hydrotreating reactions. To further validate the advantage of thin layered MWW zeolites as the metal support, the conversion rates of guaiacol on the other types of zeolites (e.g., BEA, FAU and MFI) supported Ru catalysts, which have been reported elsewhere, were estimated and used for comparison (see **Table S2**, **Figure S8** and the corresponding discussions in Supporting Information). The Ru-containing MWW zeolites as-prepared in our work, taking the bi-functional Ru@HMCM-22-IN for example, showed at least one order of magnitude higher mass-specific rates than the currently reported values in the liquid-phase HDO of guaiacol. It is noteworthy that the reaction conditions applied in the present work are much milder (3 MPa H_2, 160°C) compared to those reported studies (≥ 3 MPa H_2, 180-250°C).

3.3 Reaction pathways of HDO of guaiacol over Ru-containing MWW zeolites.

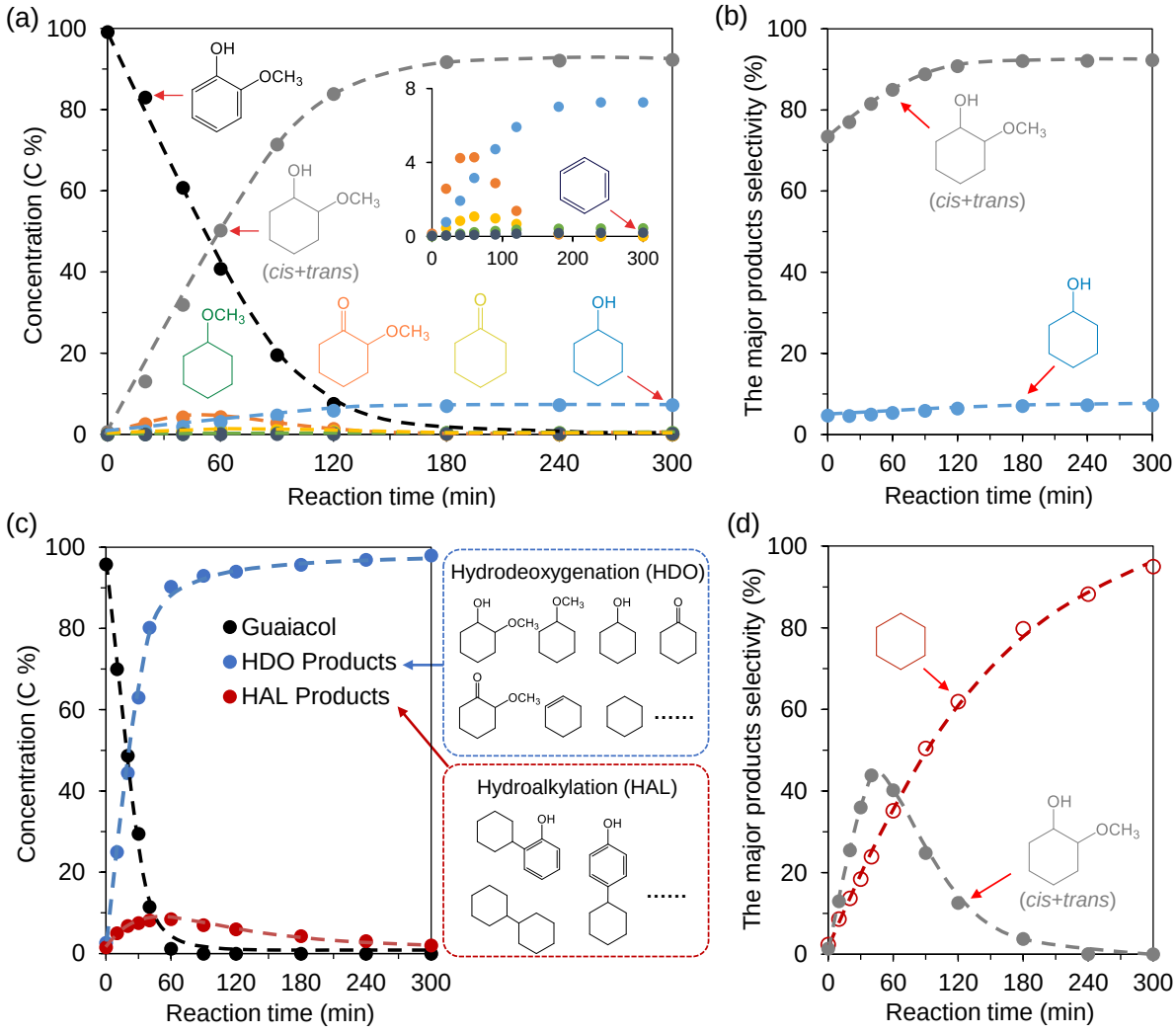

Figure 3. Time dependence of guaiacol conversion and the selectivity towards the major products of HDO of guaiacol over Ru containing MWW zeolite catalysts: (a) Carbon-based concentration-time

profiles of guaiacol and its HDO products catalyzed by mono-functional Ru@ITQ-1-IN catalyst; (b) the major products selectivity during the HDO of guaiacol over Ru@ITQ-1-IN; (c) Carbon-based concentration-time profiles of guaiacol and its HDO products catalyzed by bi-functional Ru@HMCM-22-IN catalyst; (d) the major products selectivity during the HDO of guaiacol over Ru@HMCM-22-IN. Reaction conditions: 0.30 g guaiacol, 0.10 g catalyst, 100 mL dodecane, 3 MPa H_2 (ambient temperature), stirred at 700 rpm, 160°C. Only the main components are shown here, and the correspondingly minor products with selectivity (C%) lower than 0.5 C% are not given.

Developing well-defined catalysts is critical for the fundamental understanding of chemical events that occur in the catalytic reactions. In this work, the chemistry involved in the HDO of guaiacol was detailedly investigated over mono-functional Ru@ITQ-1-IN and bi-functional Ru@HMCM-22-IN catalysts with unequivocal physicochemical properties. **Figure 3** shows the carbon-based concentration-time profiles and selectivity of the major products for the HDO of guaiacol. When Ru@ITQ-1-IN was used, hydrogenolysis and hydrogenation reactions predominately occurred, leading to the formation of 2-methoxycyclohexanol (*cis*+*trans*) and cyclohexanol as the main products with the integrated selectivity exceeding 99% after 120 min of the reaction (**Figures 3a** and **3b**). To figure out the possible reaction pathways of guaiacol over mono-functional Ru@ITQ-1-IN catalyst, the HDO of phenol and anisole, two main intermediates derived from the C-O bond scission of guaiacol, were carried out (**Figure S9**). For phenol, the cascade hydrogenation typically leads to the formation of cyclohexanol with an intermediacy of cyclohexanone, in accordance with the previous reports.[7, 25, 44, 45] For anisole, methoxycyclohexane and cyclohexanol were the major products at 100% conversion. The higher selectivity of methoxycyclohexane than cyclohexanol suggested that ring hydrogenation occurred more facilely than the C_{alkyl}-OAr bond scission during the HDO of anisole. In addition, direct deoxygenation of phenol to benzene was detectable but with a very low concentration (< 0.4 C% at 240 min) compared to that for anisole (2.2 C% at 240 min), indicating the much easier bond cleavage of C_{aryl}-OCH_3 than C_{aryl}-OH. Similarly, the higher selectivity of cyclohexanol than benzene in HDO of anisole suggested the easier bond cleavage of C_{alkyl}-OAr than C_{aryl}-OCH_3. These experimental observations were consistent with the calculated C-O bond dissociation energies in the order of C_{aryl}-OH (466 kJ mol^{-1}) > C_{aryl}-OCH_3 (409-421 kJ mol^{-1}) > C_{alkyl}-OAr (262-276 kJ mol^{-1}).[23] However, catechol was not evidently observed during the reaction of guaiacol, probably due to its much higher HDO rate under the applied conditions.[23]

When bi-functional Ru@HMCM-22-IN was used, BAS-catalyzed reactions such as dehydration and hydroalkylation (HAL) occurred, resulting in more complicated product distribution. To simplify the products analysis, HDO and HAL products were added and shown in **Figure 3c**, and the detailed product distribution can be found in **Figure S10**. In the presence

of BAS, breakage of C_{alkyl}-OH bonds (in cyclohexanol and 2-methoxycyclohexanol) via dehydration, or C_{alkyl}-OCH_3 bonds (in 2-methoxycyclohexanol) via hydrolysis, led to the complete deoxygenated product cyclohexane with the selectivity > 95% at 300 min (**Figure 3d**). Owing to the excellent activity of Ru@HMCM-22-IN in the HDO of guaiacol, the alkylated phenolic compounds were also converted to cyclohexylcyclohexane eventually (**Figure S11**). Note that HAL products first reached maxima in concentration at about 40 min and then decreased along with reaction time (**Figure 3c**). The decrease of HAL products was mainly caused by the O-alkylates (i.e., aryl ethers) which can be reversibly converted over BAS through hydrolysis[46] or elimination[47], or on Ru metal clusters through hydrogenolysis.[44, 48, 49] Based on the experimental observations, the reaction networks for HDO of guaiacol over mono- and bi-functional Ru-containing MWW zeolite catalyst were proposed in **Scheme S1**, and the detailed pathways were discussed accordingly in Supporting Information.

3.4 Enhancing the catalytic activity of Ru metal clusters through MWW zeolite pore confinement.

Next, the activity of Ru-containing catalysts synthesized by *in situ* crystallization and traditional impregnation methods were evaluated for the individual HDO of guaiacol, phenol, and anisole; thus highlighting the superiority of Ru metal clusters confined in zeolite nanopores (**Table 2**). For HDO of guaiacol, both Ru@ITQ-1-IN and Ru@HMCM-22-IN, with uniformly distributed ultra-small Ru metal clusters encapsulated inside of MWW zeolite pores, showed higher turnover rates (TOFs, obtained by normalizing the initial specific rate to the exposed Ru atoms) than Ru@ITQ-1-imp and Ru@HMCM-22-imp. In particular, Ru@HMCM-22-IN delivered almost one order of magnitude higher rates than Ru@HMCM-22-imp (1149 vs. 171 mol mol_{Ru}^{-1} h^{-1}). These results revealed the pronounced size dependence of HDO of guaiacol over Ru metal clusters, similar to the reported HDO of other lignin-derived platform molecules such as phenol and m-cresol.[50, 51] For guaiacol and anisole, TOFs were very closed over mono-functional Ru@ITQ-1-IN and bi-functional Ru@HMCM-22-IN catalysts. In contrast, Ru@HMCM-22-IN showed a differentiable rate in phenol HDO compared to that of Ru@ITQ-1-IN (13261 vs. 8462 mol mol_{Ru}^{-1} h^{-1}), indicative of a considerable contribution of BAS for phenol conversion.

Table 2. Reaction rates in the HDO of guaiacol, phenol, and anisole over the studied catalysts.

Catalyst	Reactant	TOFs[a] (mol mol_{Ru}^{-1} h^{-1})

Ru@ITQ-1-IN	Guaiacol	1126
Ru@HMCM-22-IN	Guaiacol	1149
Ru@ITQ-1-imp	Guaiacol	599
Ru@HMCM-22-imp	Guaiacol	171
Ru@ITQ-1-IN	Anisole	2049
Ru@HMCM-22-IN	Anisole	2076
Ru@ITQ-1-IN	Phenol	8462
Ru@HMCM-22-IN	Phenol	13261

[a] Turnover frequencies (TOFs) are calculated by normalizing the conversion rates of reactant molecules to the total exposed Ru atoms determined by H_2 chemisorption.

Here, we also compared the TOFs in hydrogenation and hydrogenolysis of guaiacol, anisole, and phenol over Ru@ITQ-1-IN, calculated based on the concentration-time profiles shown in **Figures 3a** and **S9**, and the proposed reaction pathways given in **Scheme S1**. As shown in **Figure 4a**, the hydrogenation was orders of magnitude faster than hydrogenolysis, especially for guaiacol and phenol with the hydrogenation/hydrogenolysis ratios > 90. This is entirely different from the results observed in the aqueous-phase reaction, in which hydrogenolysis occurred much faster than hydrogenation,[15, 23] possibly due to the significant solvent effect on reactions that occurred on the liquid-solid interface. Compared to phenol (8415 mol mol_{Ru}^{-1} h^{-1}), the much lower hydrogenation reactivity of guaiacol (1024 mol mol_{Ru}^{-1} h^{-1}) and anisole (1791 mol mol_{Ru}^{-1} h^{-1}) were attributed to the steric influence of the sp^3 methoxy group on guaiacol and anisole making the planar adsorption of the aromatic ring more difficult on Ru surface than phenol. This is also in agreement with the higher ratios of hydrogenolysis (relative to hydrogenation) for guaiacol and anisole (via the adsorption and cleavage of C_{aryl}-OCH_3 over Ru surface) than phenol, as shown in **Figure 4a**. Owing to the electron-donating effect of the adjacent hydroxyl group, easier cleavage of C_{aryl}-OCH_3 bond in guaiacol than that in anisole was expected. Indeed, a higher selectivity of cyclohexanol (~7.3%; see **Figure 4b**) while much less benzene (with a selectivity of ~ 2.2%; calculated from **Figure S9b**) was observed in the HDO of guaiacol and anisole, respectively.

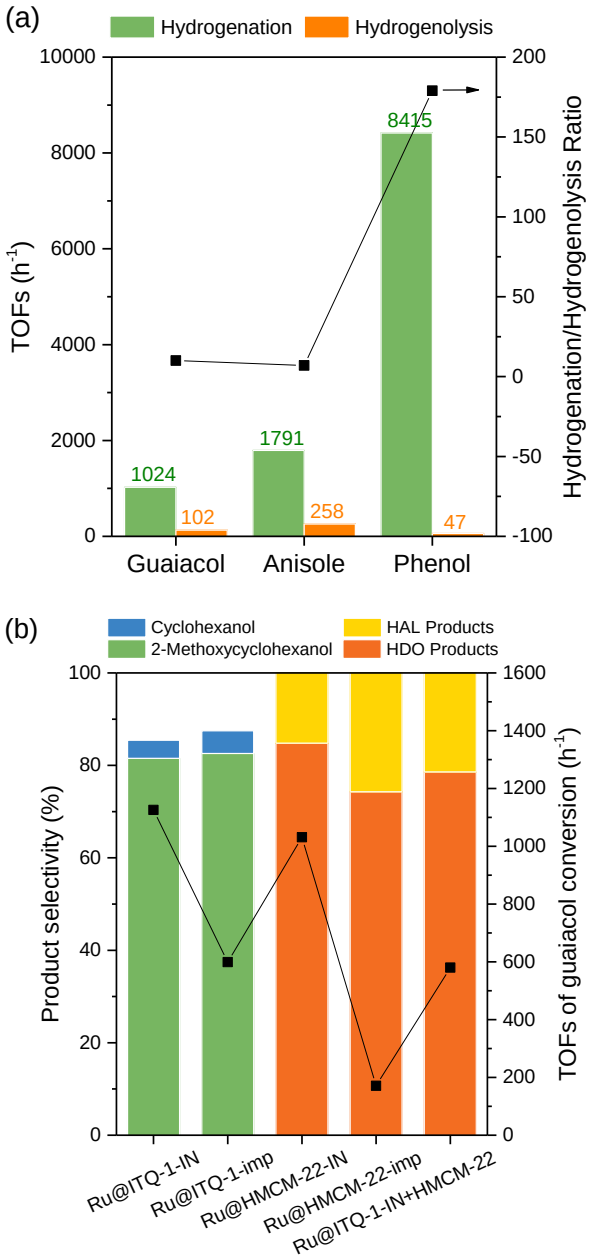

Figure 4. Reaction rates and products distribution for the HDO of guaiacol over the studied catalysts: (a) TOFs of hydrogenation and hydrogenolysis involved in the HDO of guaiacol, anisole, and phenol over Ru@ITQ-1-IN catalyst; (b) Products selectivity in the HDO of guaiacol at 40% conversion of guaiacol over the studied catalytic materials. Reaction conditions: 0.30 g guaiacol or 1.0 g phenol or 0.3 g anisole, 0.10 g Ru@ITQ-1-IN/imp or 0.10 g Ru@HMCM-22-IN/imp, 100 mL dodecane, 3 MPa H_2 (ambient temperature), stirred at 700 rpm, 160°C. A control experiment with a physical mixture of 0.10 g Ru@ITQ-1-IN with 0.080 g HMCM-22 was carried out.

In addition, the successful encapsulation of Ru metal clusters in the cavities of HMCM-22 zeolites constructed a confined microenvironment for metal and acid sites and enabled us to study the proximity effect of active sites in bi-functionally catalyzed HDO of guaiacol. On the mono-functional catalyst, Ru@ITQ-1-IN showed a twice higher turnover rate of guaiacol while comparable selectivities in the major products (i.e., 2-methoxycyclohexanol and cyclohexanol)

compared to Ru@ITQ-1-imp. Note that the difference between Ru@ITQ-1-IN and Ru@ITQ-1-imp solely originated from the size effect of Ru metal clusters. By contrast, the intimacy of Ru metal clusters and BAS on bi-functional Ru@HMCM-22-IN resulted in an order of magnitude higher turnover rate of guaiacol than Ru@HMCM-22-imp (**Figure 4b**). Thus, it is reasonable to suggest that the close proximity of metal and acid sites confined in zeolite cavities also boosts guaiacol's HDO rates over Ru@HMCM-22-IN.

We performed a control experiment using the physical mixed Ru@ITQ-1-IN and HMCM-22 to verify our hypothesis. The metal loading and the acid concentration were set as the same as those on Ru@HMCM-22-IN. A much lower TOF in the HDO of guaiacol on the mixed catalyst (841 mol mol_{Ru}^{-1} h^{-1}) than that on Ru@HMCM-22-IN (1149 mol mol_{Ru}^{-1} h^{-1}) provided direct evidence for the superior catalytic activity of Ru metal clusters being present in the vicinity of acid sites. The products distribution also reflected the advantage of metal and acid sites proximity. Due to the close proximity of Ru, BAS-catalyzed alkylation of guaiacol with its hydrodeoxygenated intermediates, i.e., alcohols and olefins, were significantly suppressed by the competitive hydrogenation and hydrogenolysis reactions, hence leading to a higher selectivity in HDO products over Ru@HMCM-22-IN. Surprisingly, Ru@ITQ-1-IN showed a lower HDO activity in the presence of physically mixed HMCM-22. This reduced activity was probably associated with the bulky alkylates formed on HMCM-22, which would re-adsorb on zeolite surface or Ru metal clusters and hinder the accessibility of the active sites on Ru@ITQ-1-IN.

3.5 Stabilizing Ru metal clusters by zeolite pore constraints.

Extensive studies have verified the merits of porous zeolite structures in protecting the metal clusters against aggregation and leaching during the liquid-phase reactions. In the present study, the durability of Ru metal clusters encapsulated in the MWW zeolites was examined by several consecutive catalytic runs of guaiacol HDO in dodecane at 160°C. For instance, bi-functional Ru@HMCM-22-IN catalysts were collected after the reaction and dried at 80°C overnight, followed by calcination at 450°C for 6 hours to remove the possibly adsorbed water and organic species. As shown in **Figure 5**, the catalytic performance of Ru@HMCM-22-IN was well maintained in terms of guaiacol conversion rates, HDO and HAL products distribution, as well as the cyclohexane selectivity after four runs of recycling (**Figure S12**). By contrast, the selectivity of HDO products declined from 74% in the first run to 67% in the fourth run over Ru@HMCM-22-imp, with the corresponding guaiacol conversion rates decreasing from 0.0025 mol g_{cat}^{-1} h^{-1} to 0.0022 mol g_{cat}^{-1} h^{-1} (**Figure S13**).

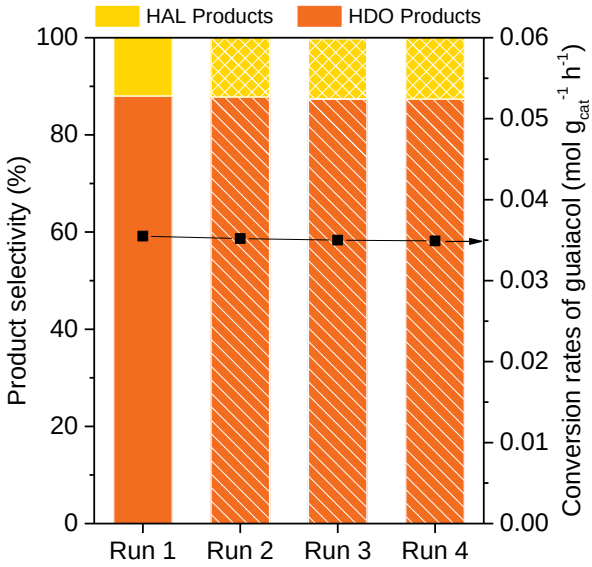

Figure 5. Durability of Ru@HMCM-22-IN catalyst in the HDO of guaiacol. Four consecutive catalytic runs were examined under the same reaction conditions: 0.30 g guaiacol, 0.10 g catalyst, 100 mL dodecane, 3 MPa H_2 (ambient temperature), stirred at 700 rpm, 160°C, 300 min. Product selectivity was obtained at about 40% conversion of guaiacol. Data comparison between the first and fourth runs, including guaiacol conversion, products yield, and cyclohexane selectivity as a function of reaction time, was given in **Figure S12**.

To track the possible changes of the catalysts, XRD, ICP-OES, and TEM were conducted for the spent Ru@HMCM-22-IN and Ru@HMCM-22-imp. As shown by XRD results (**Figure S14**), the crystallinity loss of the zeolite matrix for two catalysts was negligible, demonstrating that the decline of catalytic performance caused by the collapse of the zeolite framework could be excluded. ICP-OES analysis showed a well-retained metal content for the spent Ru@HMCM-22-IN, in line with its robust activity during consecutive catalytic runs. Conversely, about 13 wt % loss of Ru was detected for Ru@HMCM-22-imp after four catalytic runs (**Table S3**). This considerable decrease in metal loading, which might be caused by the partial leaching of much larger Ru nanoparticles on the external surface of zeolites or the ultrasmall counterparts that pore constraints cannot well stabilize, further led to the reduced catalytic activity of Ru@HMCM-22-imp in the HDO of guaiacol. After four runs of recycling, the mean size of Ru clusters remained unchanged on the pristine and spent Ru@HMCM-22-IN catalysts (see **Figures 1b** and **S15**), corroborating again the superior stability of metal clusters against sintering once they were confined in zeolite cavities.

4. CONCLUSIONS

In this study, we have successfully synthesized highly dispersed subnanometric Ru metal clusters confined in the thin layers of MWW zeolites for the low-temperature HDO of guaiacol

in the liquid phase. Compared to the impregnation method, the *in situ* hydrothermal crystallization showed great superiority in effectively encapsulating Ru metal clusters into MWW zeolites. Comprehensive characterization methods were applied to validate the size, location, dispersion, etc., of Ru metal clusters. The as-prepared Ru@ITQ-1-IN and Ru@HMCM-22-IN showed significantly enhanced catalytic performances in HDO of guaiacol in an apolar liquid media (dodecane) under mild conditions (160°C, 3 MPa H_2).

With those well-defined Ru-containing catalysts, reaction pathways, size dependence, as well as the synergistic effect between metal and acid sites in the HDO are disclosed. On Ru@ITQ-1-IN, alcohols generated either from the direct ring hydrogenation (i.e., 2-methoxycyclohexanol), or from the tandem hydrogenolysis and hydrogenation (i.e., cyclohexanol) of guaiacol, are the predominant products. When Ru@HMCM-22-IN is used, BAS-catalyzed dehydration and demethoxylation occur, leading to cyclohexane as the major product with the final selectivity exceeding 95% (at 300 min reaction). The catalytic activity of Ru is significantly boosted once they are encapsulated into zeolite cavities in the form of subnanometric clusters, indicating a prominent size dependence of Ru species for the HDO of guaiacol. This improvement is more pronounced over the bi-functional Ru@HMCM-22-IN catalyst, which can be additionally ascribed to the close proximity between Ru metal clusters and BAS within zeolite pore constraints. Moreover, zeolite encapsulated Ru metal clusters show robust hydrothermal stability against metal aggregation and leaching after successive catalytic runs of HDO in the liquid phase. The composite catalyst, subnanometric Ru metal clusters encapsulated in MWW zeolite thin layers, shows great potential in the HDO of lignin-derived phenols, and is also expected to be a good candidate for the other liquid-phase biomass valorization processes under mild conditions.

ASSOCIATED CONTENT

Supporting Information.

The Supporting Information is available free of charge at…

Characterization results; experimental data; reaction pathways; and supplementary discussions;

AUTHOR INFORMATION

Corresponding Author

Yuanshuai Liu; liuys@qibebt.ac.cn

Valentin Valtchev; valentin.valtchev@ensicaen.fr

Author Contributions

The manuscript was written with the contributions of all authors. All authors have approved the final version of the manuscript.

Notes

The authors declare no competing financial interest.

ACKNOWLEDGMENT

The authors acknowledge the start-up fund at Qingdao Institute of Bioenergy and Bioprocess Technology, Chinese Academy of Sciences. Y. Liu acknowledges the support of the National Natural Science Foundation of China (22109167) and the Shandong Provincial Natural Science Foundation Project (2022HWYQ-088). P. He acknowledges the Shandong Provincial Natural Science Foundation Project (ZR2022QB110). The authors acknowledge the collaboration in the "Sino-French International Research Network" framework.

References

(1) Abu-Omar, M.M.; Barta, K.; Beckham, G.T.; Luterbacher, J.S.; Ralph, J.; Rinaldi, R.; Román-Leshkov, Y.; Samec, J.S.M.; Sels, B.F.; Wang, F. Guidelines for performing lignin-first biorefining. *Energy Environ. Sci.* **2021**, *14*, 262-292.
(2) Renders, T.; Van den Bosch, S.; Koelewijn, S.F.; Schutyser, W.; Sels, B.F. Lignin-first biomass fractionation: the advent of active stabilisation strategies. *Energy Environ. Sci.* **2017**, *10*, 1551-1557.
(3) Rinaldi, R.; Jastrzebski, R.; Clough, M.T.; Ralph, J.; Kennema, M.; Bruijnincx, P.C.A.; Weckhuysen, B.M. Paving the way for lignin valorisation: recent advances in bioengineering, biorefining and catalysis. *Angew. Chem., Int. Ed.* **2016**, *55*, 8164-8215.
(4) Gallezot, P. Conversion of biomass to selected chemical products. *Chem. Soc. Rev.* **2012**, *41*, 1538-1558.
(5) Chheda, J.N.; Huber, G.W.; Dumesic, J.A. Liquid-phase catalytic processing of biomass-derived oxygenated hydrocarbons to fuels and chemicals. *Angew. Chem., Int. Ed.* **2007**, *46*, 7164-7183.
(6) Van den Bosch, S.; Koelewijn, S.F.; Renders, T.; Bossche, G.; Vangeel, T.; Schutyser, W.; Sels, B. F. Catalytic Strategies Towards Lignin-Derived Chemicals, Lignin Chemistry, Topics in Current Chemistry Collections. Springer, **2020**, 129-168.
(7) Saidi, M.; Samimi, F.; Karimipourfard, D.; Nimmanwudipong, T.; Gates, B.; Rahimpour, M.R. Upgrading of lignin-derived bio-oils by catalytic hydrodeoxygenation. *Energy Environ. Sci.* **2014**, *7*, 103-129.
(8) Kim, S.; Kwon, E.E.; Kim, Y.T.; Jung, S.; Kim, H.J.; Huber, G.W.; Lee, J. Recent advances in hydrodeoxygenation of biomass-derived oxygenates over heterogeneous catalysts. *Green Chem.* **2019**, *21*, 3715-3743.
(9) Roberts, V.M.; Stein, V.; Reiner, T.; Lemonidou, A.; Li, X.; Lercher, J.A. Towards quantitative catalytic lignin depolymerization. *Chem. - Eur. J.* **2011**, *17*, 5939-5948.
(10) Shangguan, J.; Hensley, A. J.; Gradiski, M. V.; Pfriem, N.; McEwen, J. S.; Morris, R. H.; Chin, Y. H. C. The role of protons and hydrides in the catalytic hydrogenolysis of guaiacol at the ruthenium nanoparticle–water interface. *ACS Catal.* **2020**, *10*, 12310-12332.
(11) Lee, E. H.; Park, R. S.; Kim, H.; Park, S. H.; Jung, S. C.; Jeon, J. K.; Kim, S.C.; Park, Y. K. Hydrodeoxygenation of guaiacol over Pt loaded zeolitic materials. *J. Ind. Eng. Chem.* **2016**, *37*, 18-21.
(12) Lu, J.; Heyden, A. Theoretical investigation of the reaction mechanism of the hydrodeoxygenation of guaiacol over a Ru(0001) model surface. *J. Catal.* **2015**, *321*, 39-50.
(13) Hong, Y. K.; Lee, D. W.; Eom, H. J.; Lee, K. Y. The catalytic activity of $Pd/WO_x/\gamma\text{-}Al_2O_3$ for hydrodeoxygenation of guaiacol. *Appl. Catal., B* **2014**, *150-151*, 438-445.
(14) Chen, M. Y.; Huang, Y. B.; Pang, H.; Liu, X. X.; Fu, Y. Hydrodeoxygenation of lignin-derived phenols into alkanes over carbon nanotube supported Ru catalysts in biphasic systems. *Green Chem.* **2015**, *17*, 1710-1717.
(15) Luo, Z.; Zheng, Z.; Wang, Y.; Sun, G.; Jiang, H.; Zhao, C. Hydrothermally stable Ru/HZSM-5-catalyzed selective hydrogenolysis of lignin-derived substituted phenols to bio-arenes in water. *Green Chem.* **2016**, *18*, 5845-5858.
(16) Wang, L.; Zhang, J.; Yi, X.; Zheng, A.; Deng, F.; Chen, C.;Ji, Y.; Liu, F.; Xiao, F. S. Mesoporous ZSM-5 zeolite-supported Ru nanoparticles as highly efficient catalysts for upgrading phenolic biomolecules. *ACS Catal.* **2015**, *5*, 2727-2734.
(17) Yan, P.; Kennedy, E.; Stockenhuber, M. Hydrodeoxygenation of guiacol over ion-exchanged ruthenium ZSM-5 and BEA zeolites. *J. Catal.* **2021**, *396*, 157-165.
(18) Colmenares, J. C.; Varma, R. S.; Nair, V. Selective photocatalysis of lignin-inspired chemicals by integrating hybrid nanocatalysis in microfluidic reactors. *Chem. Soc. Rev.* **2017**, *46*, 6675-6686.
(19) Ennaert, T.; Van Aelst, J.; Dijkmans, J.; De Clercq, R.; Schutyser, W.; Dusselier, M.; Verboekend, D.; Sels, B. F. Potential and challenges of zeolite chemistry in the catalytic conversion of biomass. *Chem. Soc. Rev.* **2016**, *45*, 584-611.
(20) Kubička, D.; Kikhtyanin, O. Opportunities for zeolites in biomass upgrading—Lessons from the refining and petrochemical industry. *Catal. Today* **2015**, *243*, 10-22.
(21) Liu, L.; Corma, A. Confining isolated atoms and clusters in crystalline porous materials for catalysis. *Nat. Rev. Mater.* **2021**, *6*, 244-263.

(22) Wang, Y.; Wang, C.; Wang, L.; Wang, L.; Xiao, F. S. Zeolite fixed metal nanoparticles: new perspective in catalysis. *Acc. Chem. Res.* **2021**, *54*, 2579-2590.
(23) Song, W.; Liu, Y.; Baráth, E.; Zhao, C.; Lercher, J. A. Synergistic effects of Ni and acid sites for hydrogenation and C–O bond cleavage of substituted phenols. *Green Chem.* **2015**, *17*, 1204-1218.
(24) He, J.; Wu, Z.; Gu, Q.; Liu, Y.; Chu, S.; Chen, S.; Zhang,Y.; Yang, B.; Chen, T.; Wang, A.; Weckhuysen, B.M.; Zhang, T.; Luo, W. Zeolite-tailored active site proximity for the efficient production of pentanoic biofuels. *Angew. Chem., Int. Ed.* **2021**, *133*, 23906-23914.
(25) Yang, J.; He, Y.; He, J.; Liu, Y.; Geng, H.; Chen, S.; Lin, L.; Liu, M.; Chen, T.; Jiang, Q.; Weckhuysen, B.M.; Luo, W.; Wu, Z. Enhanced catalytic performance through in situ encapsulation of ultrafine Ru clusters within a high-aluminum zeolite. *ACS Catal.* **2022**, *12*, 1847-1856.
(26) Wang, N.; Sun, Q.; Zhang, T.; Mayoral, A.; Li, L.; Zhou, X.; Xu, J.; Zhang P.; Yu, J. Impregnating subnanometer metallic nanocatalysts into self-pillared zeolite nanosheets. *J. Am. Chem. Soc.* **2021**, *143*(18), 6905-6914.
(27) Han, J.; Cho, J.; Kim, J. C.; Ryoo, R. Confinement of supported metal catalysts at high loading in the mesopore network of hierarchical zeolites, with access via the microporous windows. *ACS Catal.* **2018**, *8*(2), 876-879.
(28) Mintova, S.; Gilson, J. P.; Valtchev, V. Advances in nanosized zeolites. *Nanoscale*, **2013**, *5*(15) 6693-6703.
(29) Ma, B.; Zhao, C. High-grade diesel production by hydrodeoxygenation of palm oil over a hierarchically structured Ni/HBEA catalyst. *Green Chem.* **2015**, *17*(3), 1692-1701.
(30) Ma, B.; Yi, X.; Chen, L.; Zheng, A.; Zhao, C. Interconnected hierarchical HUSY zeolite-loaded Ni nano-particles probed for hydrodeoxygenation of fatty acids, fatty esters, and palm oil. *J. Mater. Chem. A*, **2016**, *4*(29), 11330-11341.
(31) Choi, M.; Na, K.; Kim, J.; Sakamoto, Y.; Terasaki, O.; Ryoo, R. Stable single-unit-cell nanosheets of zeolite MFI as active and long-lived catalysts. *Nature*, **2009**, *461*(7261), 246-249.
(32) Dai, W.; Kouvatas, C.; Tai, W.; Wu, G.; Guan, N.; Li, L.; Valtchev, V. Platelike MFI crystals with controlled crystal faces aspect ratio. *J. Am. Chem. Soc.* **2021**, *143*(4), 1993-2004.
(33) Corma, A.; Martınez-Soria, V.; Schnoeveld, E. Alkylation of benzene with short-chain olefins over MCM-22 zeolite: catalytic behaviour and kinetic mechanism. *J. Catal.* **2000**, *192*(1), 163-173.
(34) Wu, Y.; Lu, Z.; Emdadi, L.; Oh, S. C.; Wang, J.; Lei, Y.; Chen, H.; Dran, D. T.; Lee, I. C.; Liu, D. Tuning external surface of unit-cell thick pillared MFI and MWW zeolites by atomic layer deposition and its consequences on acid-catalyzed reactions. *J. Catal.* **2016**, *337*, 177-187.
(35) Wang, N.; Sun, Q.; Yu, J. Ultrasmall metal nanoparticles confined within crystalline nanoporous materials: a fascinating class of nanocatalysts. *Adv. Mater.* **2019**, *31*, 1803966.
(36) Wang, N.; Sun, Q.; Bai, R.; Li, X.; Guo, G.; Yu, J. In situ confinement of ultrasmall Pd clusters within nanosized silicalite-1 zeolite for highly efficient catalysis of hydrogen generation. *J. Am. Chem. Soc.* **2016**, *138*, 7484-7487.
(37) Sun, Q.; Wang, N.; Bai, R.; Hui, Y.; Zhang, T.; Do, D. A.; Zhang, P.; Song, L.; Miao, S.; Yu, J. Synergetic effect of ultrasmall metal clusters and zeolites promoting hydrogen generation. *Adv. Sci.* **2019**, *6*, 1802350.
(38) Singh, K.S.W.; Rouquerol, J.; Bergeret, G.; Gallezot, P.; Vaarkamp, M.; Koningsberger, D.C.; Datye, A.K.; Niemantsverdriet, J.W.; Butz, T.; Engelhardt, G.; Mestl, G.; Knözinger, H.; Jobic, H. Characterization of Solid Catalysts: Sections 3.1.1 – 3.1.3, in: Handbook of Heterogeneous Catalysis, **1997**, 427-582.
(39) Kim, K. S.; and Winograd. N. X-Ray photoelectron spectroscopic studies of ruthenium-oxygen surfaces. *J. Catal.* **1974**, *35*(1), 66-72.
(40) Rutkowska, M.; Díaz, U.; Palomares, A.E.; L.Chmielarz, L. Cu and Fe modified derivatives of 2D MWW-type zeolites (MCM-22, ITQ-2 and MCM-36) as new catalysts for DeNOx process. *Appl. Catal., B* **2015**, *168*, 531-539.
(41) Souverijns, W.; Verrelst, W.; Vanbutsele, G.; Martens, J. A.; Jacobs, P. A. Micropore structure of zeolite MCM-22 as determined by the decane catalytic test reaction. *J. Chem. Soc., Chem. Commun.* **1994**, 1671-1672.
(42) Gutiérrez-Rubio, S.; Berenguer, A.; Přech, J.; Opanasenko, M.; Ochoa-Hernández, C.; Pizarro, P.; Čejka, J.; Serrano, D. P.; Coronado, J. M.; Moreno, I. Guaiacol hydrodeoxygenation over Ni2P supported on 2D-zeolites. *Catal. Today*, **2020**, *345*, 48-58.

(43) Güray, I.; Warzywoda, J.; Bac, N.; Sacco Jr, A. Synthesis of zeolite MCM-22 under rotating and static conditions. *Microporous Mesoporous Mater.* **1999**, *31*(3), 241-251.
(44) Yao, G.; Wu, G.; Dai, W.; Guan, N.; Li, L. Hydrodeoxygenation of lignin-derived phenolic compounds over bi-functional Ru/H-Beta under mild conditions. *Fuel*, **2015**, *150*, 175-183.
(45) Wang, X.; Arai, M.; Wu, Q.; Zhang, C.; Zhao, F. Hydrodeoxygenation of lignin-derived phenolics – a review on the active sites of supported metal catalysts. *Green Chem.* **2020**, *22*, 8140-8168.
(46) Liu, Y.; Barath, E.; Shi, H.; Hu, J.; Camaioni, D. M.; Lercher, J. A. Solvent-determined mechanistic pathways in zeolite-H-BEA-catalysed phenol alkylation. *Nat. Catal.* **2018**, *1*, 141-147.
(47) John, M.; Alexopoulos, K.; Reyniers, M. F.; Marin, G. B. Reaction path analysis for 1-butanol dehydration in H-ZSM-5 zeolite: Ab initio and microkinetic modeling. *J. Catal.* **2015**, *330*, 28-45.
(48) Zaheer, M.; Kempe, R. Catalytic hydrogenolysis of aryl ethers: a key step in lignin valorization to valuable chemicals. *ACS Catal.* **2015**, *5*, 1675-1684.
(49) Schmid, J.; Wang, M.; Gutiérrez, O. Y.; Bullock, R. M.; Camaioni, D. M.; Lercher, J. A. Controlling reaction routes in noble-metal-catalyzed conversion of aryl ethers. *Angew. Chem., Int. Ed.* **2022**, *134*(30), e202203172.
(50) Mortensen, P. M.; Grunwaldt, J. D.; Jensen, P. A.; Jensen, A. D. Influence on nickel particle size on the hydrodeoxygenation of phenol over Ni/SiO_2. *Catal. Today* **2016**, *259*, 277-284.
(51) Yang, F.; Liu, D.; Zhao, Y.; Wang, H.; Han, J.; Ge, Q.; Zhu, X. Size dependence of vapor phase hydrodeoxygenation of m-cresol on Ni/SiO_2 catalysts. *ACS Catal.* **2018**, *8*, 1672-1682.

For Table of Contents Only